

An Accurate Nonuniform Fourier Transform for SPRITE Magnetic Resonance Imaging Data

J. RIOUX, M. HALSE, E. AUBANEL, and B. J. BALCOM

University of New Brunswick

and

J. KAFFANKE, S. ROMANZETTI, T. DIERKES, and N. J. SHAH

MR Group, IME Forschungszentrum Juelich

A new algorithm is proposed for computing the discrete Fourier Transform (DFT) of purely phase encoded data acquired during Magnetic Resonance Imaging (MRI) experiments. These experiments use the SPRITE (Single Point Ramped Imaging with T_1 Enhancement) method and multiple-point acquisition, sampling data in a nonuniform manner that prohibits reconstruction by fast Fourier transform. The chirp z-transform algorithm of Rabiner, Schafer, and Rader can be combined with phase corrections to compute the DFT of this data to extremely high accuracy. This algorithm outperforms the interpolation methods that are traditionally used to process nonuniform data, both in terms of execution time and in terms of accuracy as compared to the DFT.

Categories and Subject Descriptors: F.2.1 [Analysis of Algorithms and Problem Complexity]: Numerical Algorithms and Problems—*Computation of transforms*; I.4.5 [Image Processing and Computer Vision]: Reconstruction—*Transform methods*; J.2 [Physical Sciences and Engineering]—*Physics*

General Terms: Algorithms, Performance

B. J. Balcom thanks NSERC of Canada for operating and equipment grants, and thanks the Canada Chairs program for a Research Chair in MRI of Materials (2002–2009). J. Rioux thanks the UNB Computer Science co-op program for summer work placements. M. Halse thanks NSERC of Canada for a post-graduate scholarship, UNB for a John S. Little International Study Fellowship and Forschungszentrum Jülich for a travel grant. The UNB MRI Centre is supported by an NSERC Major Facilities Access grant. The 4T facility in Jülich is funded by the DFG (ZI 192/14-1) and the BMBF (01GO0104 and 01GO0204). We thank Michel F. Couturier, UNB Chemical Engineering, for the polyester sample.

Authors' addresses: J. Rioux, NRC-IBD (Atlantic), 1796 Summer Street, Suite 3900, Halifax NS, B3H 3A7, Canada; M. Halse, E. Aubanel, and B. J. Balcom, University of New Brunswick, PO Box 4400, Fredericton NB, E3B 5A3, Canada; J. Kaffanke, S. Romanzetti, T. Dierkes, and N. J. Shah, MR Group, IME Forschungszentrum Juelich, D-52425, Juelich, Germany. Direct correspondence to E. Aubanel at aubanel@unb.ca.

Permission to make digital or hard copies of part or all of this work for personal or classroom use is granted without fee provided that copies are not made or distributed for profit or direct commercial advantage and that copies show this notice on the first page or initial screen of a display along with the full citation. Copyrights for components of this work owned by others than ACM must be honored. Abstracting with credit is permitted. To copy otherwise, to republish, to post on servers, to redistribute to lists, or to use any component of this work in other works requires prior specific permission and/or a fee. Permissions may be requested from Publications Dept., ACM, Inc., 2 Penn Plaza, Suite 701, New York, NY 10121-0701 USA, fax +1 (212) 869-0481, or permissions@acm.org.
© 2007 ACM 0098-3500/2007/08-ART16 \$5.00 DOI 10.1145/1268769.1268770 <http://doi.acm.org/10.1145/1268769.1268770>

Additional Key Words and Phrases: Discrete Fourier transform, nonuniform Fourier transform, chirp z-transform, MRI, SPRITE

ACM Reference Format:

Rioux, J., Halse, M., Aubanel, E., Balcom, B. J., Kaffanke, J., Romanzetti, S., Dierkes, T., and Shah, N. J. 2007. An accurate nonuniform Fourier transform for SPRITE magnetic resonance imaging data. *ACM Trans. Math. Softw.* 33, 3, Article 16 (August 2007), 21 pages. DOI = 10.1145/1268769.1268770 <http://doi.acm.org/10.1145/1268769.1268770>

1. INTRODUCTION

The fast Fourier transform (FFT) algorithm of Cooley and Tukey [1965] provides an accurate way to evaluate the discrete Fourier transform (DFT) of a sequence of N uniformly spaced samples in $O(N \log N)$ time. In general, neither the speed nor the accuracy of the FFT can be duplicated in the case of nonuniformly sampled data. Algorithms to evaluate the DFT for nonuniform data typically employ an approximation scheme, with increased accuracy available at the cost of increased execution time.

One application of the nonuniform fast Fourier transform is in the reconstruction of magnetic resonance imaging (MRI) data. Imaging methods used in clinical settings often sample data in non-Cartesian trajectories [Meyer et al. 1992], and the resulting images must be processed by a nonuniform Fourier transform. Images of materials acquired with SPRITE (Single Point Ramped Imaging with T_1 Enhancement) [Balcom et al. 1996] or any of its centric-scan variants [Halse et al. 2003] can also acquire nonuniformly sampled data. Some of the methods that can be used to process this data include convolution regridding [Jackson et al. 1991], the Dutt-Rokhlin interpolation method [Dutt and Rokhlin 1993] and its 2-D generalization [Sarty et al. 2001], or the interpolation method of Sha, Guo, and Song [2003], which is based on the regular Fourier matrices of Liu and Nguyen [1998, 1999].

Another method which has recently been proposed for reconstructing certain types of nonuniform data is based upon the chirp z-transform (CZT) of Rabiner et al. [1969]. Kaffanke et al. [2005] have explored the application of the CZT to MRI data following the initial work of Halse et al. [2004] and Rioux [2003]. It has been shown that nonuniformly sampled SPRITE images, reconstructed with the CZT, exhibit greater apparent resolution and substantially higher SNR than the corresponding uniformly sampled image, but are acquired and processed in the same amount of time.

In the current paper we explore the implementation of an algorithm that combines the CZT with appropriate phase corrections to compute the DFT to very high precision. This can be used to reconstruct nonuniformly sampled SPRITE MRI data with the same level of computational complexity as the FFT, and with an accuracy that matches the DFT to within the double-precision machine epsilon ($\epsilon \sim 10^{-16}$) for most one-dimensional computations. We then compare the performance of this algorithm to a widely used interpolation method.

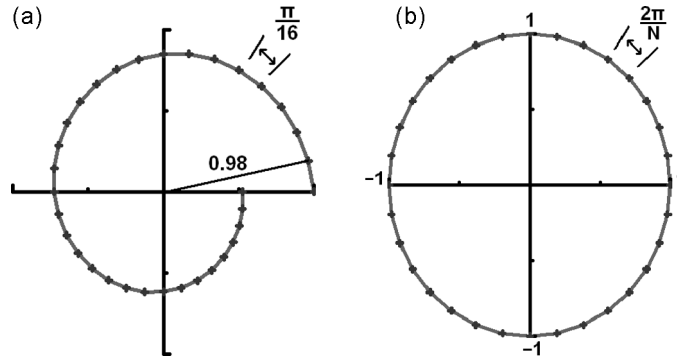


Fig. 1. (a) A typical z-plane contour, described by $z(k) = 0.98^k e^{\pi i k / 16}$. (b) The z-plane contour equivalent to the DFT, $z(k) = e^{2\pi i k / N}$.

2. THEORY

In this section we shall outline the mathematical basis of the Chirp z-Transform algorithm, following the example of Rabiner et al. [1969]. We will also briefly outline the fundamentals of Magnetic Resonance Imaging theory, to show why the Fourier relationship is important to the reconstruction of the MRI image, and why certain imaging techniques require a nonuniform Fourier transform.

2.1 Chirp Z-Transform

The Fourier transform is a special case of the more general z-transform, defined as

$$X(z) = \sum_{n=-\infty}^{\infty} x_n z^{-n} \quad (1)$$

for a sequence of numbers x_n , where z , x_n , and $X(z)$ are all complex. In the discrete case, there are a finite number N of samples, and the transform is computed at a finite number M of values, z_k . That is to say,

$$X(z_k) = \sum_{n=0}^{N-1} x_n z_k^{-n} \quad k \in \{0, 1, \dots, M-1\}. \quad (2)$$

The values z_k describe a contour in the z-plane (see Figure 1). For example, the choice of contour $z_k = e^{2\pi i k / N}$ allows us to recover the form of the DFT:

$$X(z_k) = \sum_{n=0}^{N-1} x_n e^{-2\pi i n k / N}. \quad (3)$$

We will now demonstrate that the z-transform along a certain family of contours is expressible in terms of a convolution of two sequences, and can therefore be computed at high speed using the FFT and the convolution theorem. This family of contours is described by

$$z_k = A W^{-k}, \quad A = A_0 e^{i\theta_0}, \quad W = W_0 e^{i\phi_0}. \quad (4)$$

This contour begins at a distance A_0 from the origin and at an angular displacement of θ_0 from the horizontal axis. The contour circles the origin (if $W_0 = 1$),

spirals inward (if $W_0 < 1$), or spirals outward (if $W_0 > 1$), with samples spaced at angular intervals of ϕ_0 (see Figure 1).

Rabiner et al. [1969] showed that, along this contour, the z-transform can be reformulated in terms of a convolution, using the substitution $nk = \frac{n^2+k^2-(k-n)^2}{2}$ [Bluestein 1968] as follows:

$$X(z_k) = \sum_{n=0}^{N-1} x_n A^{-n} W^{nk} \quad k \in \{0, 1, \dots, M-1\} \quad (5)$$

$$= \sum_{n=0}^{N-1} x_n A^{-n} W^{n^2/2} W^{k^2/2} W^{-(k-n)^2/2} \quad (6)$$

$$= W^{k^2/2} \sum_{n=0}^{N-1} (x_n A^{-n} W^{n^2/2}) (W^{-(k-n)^2/2}) \quad (7)$$

$$= W^{k^2/2} ((x_n A^{-n} W^{n^2/2}) \otimes (W^{-n^2/2}))_k. \quad (8)$$

The convolution theorem states that a convolution in a given space is equivalent to a multiplication in the appropriate Fourier space. The above convolution can therefore be computed in $O(N \log N)$ time using a combination of FFT operations. The algorithm for performing this computation is described in Section 3, and was named the “chirp z-transform” by Rabiner et al. [1969] since the function $W^{n^2/2}$ found in the expression is a sinusoid called a “chirp” in radar applications.

2.2 Magnetic Resonance Imaging

The phenomenon of nuclear magnetic resonance (NMR) occurs in atomic nuclei having a net magnetic dipole moment. When placed inside an external magnetic field of magnitude B_0 , these nuclei will be separated into distinct energy levels, at a separation of

$$\Delta E = \hbar \gamma B_0 = \hbar \omega_0. \quad (9)$$

The gyromagnetic ratio γ is characteristic of the nucleus; for example, the hydrogen nucleus has $\gamma = 42.6$ MHz/T. The quantity $\omega_0 = \gamma B_0$ is called the Larmor frequency. This describes the rate at which the nuclei precess or spin about the magnetic field lines, in the same manner that a gyroscope spins in a gravitational field.

The population of the energy levels is such that the sample acquires a net magnetization in the direction parallel to the applied magnetic field. Providing the system with energy at the Larmor frequency—for example, by applying a radio-frequency (RF) pulse at that precise frequency—rotates this magnetization into the transverse plane, where it is free to precess at the Larmor frequency. The resulting time-dependent magnetization will induce a voltage into a suitably oriented receiver coil, creating the MRI signal.

This yields information about the bulk properties of the material being examined, and for chemical or spectroscopic analysis of the sample we need proceed no further. However, to obtain an image with spatial resolution in a given direction (say, \hat{x}), a magnetic field gradient $\vec{G}_x = \frac{d\vec{B}_0}{dx}$ can be applied across the

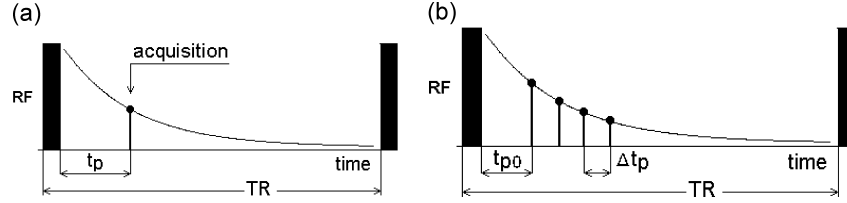


Fig. 2. (a) A single point acquisition following the RF pulse, after an encoding time t_p . (b) A multiple point acquisition with $N_T = 4$.

sample, such that the Larmor frequency acquires a spatial dependence,

$$\omega(x) = \gamma(B_0 + G_x x). \quad (10)$$

Different regions of the sample will now induce voltages at different frequencies, and the total received signal can be expressed as an integral over all space:

$$s(t) = \int_{-\infty}^{+\infty} \rho(x) e^{i\omega(x)t} dx. \quad (11)$$

The complex exponential is used to account for the precessing magnetization, while $\rho(x)$ is the nuclear density as a function of position. Using Equation (10), and ignoring the constant term $e^{i\gamma B_0 t}$ yields

$$s(t) = \int_{-\infty}^{+\infty} \rho(x) e^{i\gamma x G_x t} dx, \quad (12)$$

which through the change of variables $k = \gamma G t / 2\pi$ becomes

$$S(k) = \int_{-\infty}^{+\infty} \rho(x) e^{2\pi i k x} dx. \quad (13)$$

This describes a Fourier relationship between the nuclear density of the sample as a function of position, and the intensity of the signal $S(k)$ acquired in the so-called k-space. The MRI experiment then consists of sampling k-space and applying a Fourier transform to reconstruct the desired image [Paschal and Morris 2004].

2.3 SPRITE and Multiple Point Acquisition

The lifetime of the signal that gives rise to an MRI image depends on the properties of the material being imaged. In most medical contexts, where the material of interest is human tissue, signal decay times are generally quite long, on the order of a second. In the study of materials, the signal decays much more rapidly (a difference of up to four orders of magnitude). The techniques which are best suited for producing images of materials will be quite different from those used in medical contexts, since they must be unaffected by this rapid decay. One such technique is SPRITE [Balcom et al. 1996].

This technique samples k-space by changing the magnitude of the magnetic field gradient \vec{G} in small steps $\Delta \vec{G}$, and at each step applying an RF pulse. The resulting signal is then sampled, as depicted in Figure 2(a); usually a single point is acquired at a specific time after the RF pulse, called the encoding time

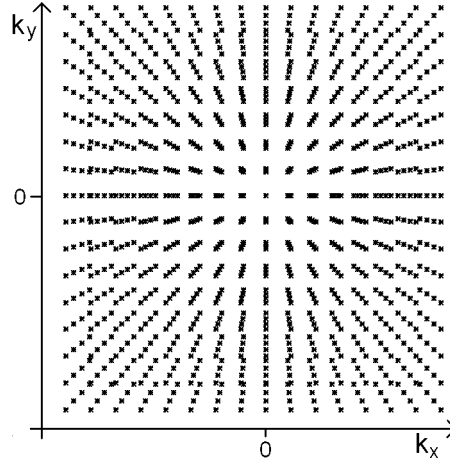


Fig. 3. Nonuniform k-space sampling pattern for SPRITE with rectilinear sampling ($N_G = 16$) and multiple point acquisition ($N_T = 4$). Despite nonuniformity, the pattern clearly consists of a number of superimposed uniform grids, and this enables processing by the chirp z-transform.

t_p . The k-space sampling pattern can be rectilinear or spiral-shaped, though in both cases the sampled locations are chosen such that they fall on the Cartesian grid, enabling processing with the FFT.

It is also possible to acquire multiple samples of the decaying MRI signal; for example, N_T points may be acquired at times

$$t_p(j) = t_{p0} + j \Delta t_p, 0 \leq j < N_T, \quad (14)$$

with the spacing Δt_p on the order of a microsecond. (See Figure 2(b).) The signal intensity of most materials will not decrease appreciably during this short interval. This will not contribute to the overall acquisition time, but each sample provides additional information about the image, and if these data could somehow be combined, the resulting final image would be of higher quality.

Despite the potential benefits, multiple-point acquisition is not widely practiced with these techniques because of difficulties encountered in data processing [Prado et al. 1999]. The resulting dataset is no longer uniformly spaced and cannot be processed with the FFT. (See Figure 3.) Attempts to separate the data into uniform sets acquired at each time value $t_p(j)$ yield a number of different images, each having a different field of view, given by

$$FOV(j) = 1/\Delta k = 2\pi/\gamma \Delta G t_p(j). \quad (15)$$

These images cannot be combined without correcting the fields of view such that all images have a common FOV. To maximize resolution we generally correct all images to the smallest FOV, scaling them by a factor of

$$T_j = \frac{FOV_{min}}{FOV_j} = \frac{t_p(j)}{t_{max}}, \quad (16)$$

with t_{max} the longest encoding time used (corresponding to the minimum FOV).

In practice, there is a limit on the number of points that can be collected for the purposes of signal averaging [Halse et al. 2004]. This number depends both

on the k-space matrix size N_G and the desired limit on FOV scaling, T_{lim} , as

$$n \leq \frac{N_G}{2} \left(\frac{1}{T_{lim}} - 1 \right) + 1. \quad (17)$$

In most practical applications we require $T_{lim} \geq 0.8$ to maintain acceptable resolution; the maximum number of samples for $N_G = 64$ is then found to be 9.

It has recently been shown that the chirp z-transform algorithm provides a suitable mechanism for properly correcting the fields of view of multiple point SPRITE data, such that the images can be combined to improve overall SNR [Halse et al. 2004]. In the remainder of this paper we will demonstrate the equivalent claim, that the chirp z-transform can be used to compute the DFT of this data with the same complexity as the FFT.

2.4 The DFT for SPRITE Data

Replacing the integral in equation (13) above with a discrete summation and applying a discrete Fourier transform yields

$$\sum_{n=0}^{N_C-1} s(k_n) e^{-2\pi i k_n x_m} = \sum_{n=0}^{N_C-1} \rho(x_m) K(x_n - x_m), \quad (18)$$

where N_C represents the total number of collected samples, and $K(\cdot)$ is a convolution kernel that depends on the nonuniformity of the points k_n . For uniformly distributed k_n , $K = \delta_n^m$, the Kronecker delta. In the case of the experiments considered in the paper, since all the data at a given time point are uniform, approximating K to a Kronecker delta is also valid, and therefore we assume

$$\sum_{n=0}^{N_C-1} s(k_n) e^{-2\pi i k_n x_m} = \rho(x_m) \quad m \in \{0, 1, \dots, N_C - 1\}. \quad (19)$$

Our next goal is to modify this equation to make it somewhat more appropriate for the multiple-point acquisition SPRITE experiments of the previous section. We shall restrict ourselves to a single dimension, with the understanding that these results can easily be generalized to higher dimensions.

First we reverse the substitution which led to equation (13), restoring explicit dependence on the gradient G and the time t and converting a single summation into a double summation.

$$\rho(x_m) = \sum_{j=0}^{N_T-1} \sum_{k=0}^{N_G-1} s(G_k t_p(j)) e^{-i\gamma x_m G_k t_p(j)}, \quad (20)$$

N_G is the number of gradient steps in the SPRITE pulse sequence, and N_T is the number of samples of the decaying MRI signal at each step. The total number of collected samples, and the total number of calculated $\rho(x)$ values, remains $N_C = N_G N_T$.

To simplify the implementation and algebraic manipulations, we will map the values of the complex exponential into the range $[-\pi N_G, \pi N_G]$ by the

following modification:

$$\rho(x_m) = \sum_{j=0}^{N_T-1} \sum_{k=0}^{N_G-1} s(G_k t_p(j)) e^{-i\theta}, \quad (21)$$

$$\theta = \pi N_G (x_m/x_{max})(G_k/G_{max})(t_p(j)/t_{max}), \quad (22)$$

x_{max} represents the largest value of the position coordinate, G_{max} is the maximum value of the magnetic field gradient, and $t_{max} = t_{p0} + (N_T - 1)\Delta t_p$ is the longest encoding time. The dependence on γ has also been removed since it introduces only a constant scaling factor.

It can be verified by inspection that θ now takes on values between $-\pi N_G$ and $+\pi N_G$, since the position x and encoding time t have been scaled into the range $[0, 1]$, while the gradient value has been scaled into the range $[-1, 1]$.

For a SPRITE experiment, the following is true of the gradient values G_k :

$$\begin{aligned} G_k &= -G_{max} + k \Delta G, \\ \Delta G &= 2G_{max}/N_G, \\ \therefore G_k/G_{max} &= 2k/N_G - 1. \end{aligned}$$

This allows us to further simplify the expression above by removing the dependence on G_{max} . To eliminate the need to shift the final result by $N_C/2$ pixels when the operation is complete, we will also set $(x_m/x_{max}) = (m/N_C - 1/2)$. Now $m = 0$ corresponds to $x = -\frac{1}{2}$ while $m = N_C$ would correspond to $x = +\frac{1}{2}$. Again, this does not change the validity of the expression, only the ease with which it can be interpreted.

Incorporating these changes into the DFT of equation (22) yields the final form of the discrete Fourier transform for SPRITE data with multiple-point acquisition:

$$\rho(x_m) = \sum_{j=0}^{N_T-1} \sum_{k=0}^{N_G-1} s(G_k t_p(j)) e^{-i\theta} \quad m \in \{0, 1, \dots, N_C - 1\} \quad (23)$$

$$\theta = 2\pi N_G (m/N_C - 1/2)(k/N_G - 1/2)(t_p(j)/t_{max}) \quad (24)$$

2.5 Computing the DFT with a Chirp Z-Transform

To conclude this section we demonstrate that equation (23) is equivalent to a series of chirp z-transforms, with a suitable choice of contour, and subsequent phase corrections.

We shall make use of the same contour used to correct the fields of view for multiple-point data in Halse et al. [2004]:

$$A = e^{-\pi i T_j}, \quad W = e^{-2\pi i T_j/N_C} \quad (25)$$

where we have used, as before, $T_j = t_p(j)/t_{max}$. This will scale the FOV of the j^{th} image to match the FOV of the final image (with $j = N_T - 1$). Again, this choice ensures that the final combined image has the smallest possible field of view, and the highest resolution.

For each image we then obtain a different chirp z-transform, of the form

$$CZT(x_m, t_p(j)) = \sum_{k=0}^{N_G-1} s(G_k t_p(j)) e^{\pi i k T_j} e^{-2\pi i k m T_j / N_C} \quad (26)$$

and to create a single combined image, we simply sum over all N_T images:

$$\rho(x_m) = \sum_{j=0}^{N_T-1} CZT(x_m, t_p(j)) \quad (27)$$

$$= \sum_{j=0}^{N_T-1} \sum_{k=0}^{N_G-1} s(G_k t_p(j)) e^{\pi i k T_j} e^{-2\pi i k m T_j / N_C}. \quad (28)$$

Compare this with our earlier formulation of the DFT (equations (23) and (24)). We can make these two expressions exactly equivalent by ensuring that the arguments of the exponential are equal. Expanding the exponent in (24) yields

$$\begin{aligned} \theta &= -2\pi i N_G (m/N_C - 1/2)(k/N_G - 1/2)T_j \\ &= -2\pi i N_G T_j (k m / N_C N_G - k/2N_G - m/2N_C + 1/4) \\ &= -2\pi i T_j k m / N_C + \pi i k T_j + \pi i T_j m / N_T - \pi i N_G T_j / 2. \end{aligned}$$

The first two terms of this expansion match the existing argument in equation (28). To account for the remaining terms we add to equation (27) a pair of phase corrections:

$$\rho(x_m) = \sum_{j=0}^{N_T-1} CZT(x_m, t_p(j)) e^{i(\alpha m + \beta)}, \quad (29)$$

with the linear phase correction $\alpha = \pi T_j / N_T$ and global phase correction $\beta = -\pi N_G T_j / 2$.

This demonstrates that an appropriate choice of phase corrections and contour parameters allows us to compute the discrete Fourier transform for multiple-point SPRITE data using a sum of chirp z-transforms.

3. ALGORITHMS

This section contains descriptions of the chirp z-transform algorithm, a one-dimensional algorithm for properly FOV-correcting and combining SPRITE MRI data using the CZT, and the generalization of this algorithm to higher dimensions. Theoretical running time analysis is also performed on each algorithm, with experimental confirmation in Section 4.

In all cases these algorithms have been implemented in IDL (Interactive Data Language) 6.0, a product of Research Systems, Inc. Our implementation of the CZT is based upon the `czt` function in Matlab's Signal Processing Toolbox, with no further optimization added.

3.1 Implementation of the CZT

Our implementation of the Chirp Z-Transform generally follows the example of Rabiner et al. [1969], with some minor modifications to suit our desired application.

Algorithm 1. (Computation of 1D Chirp Z-Transform).

INPUT: \mathbf{X} , an N_G -element vector of SPRITE MPA data
 INPUT: N , an integer specifying the desired size of transform
 INPUT: T , a scaling factor ($0 < T \leq 1$)
 OUTPUT: The N -point Chirp Z-Transform of the dataset \mathbf{X}
 $L = 2N$
 $W = e^{2\pi T/N}$
 $A = e^{-\pi T}$
 let \mathbf{Y} and \mathbf{V} be empty L -element vectors
 for $i = 0$ to $N_G - 1$ do $\mathbf{Y}[i] = A^{-i} * W^{i^2/2} * \mathbf{X}[i]$
 for $i = 0$ to $N - 1$ do $\mathbf{V}[i] = W^{-i^2/2}$
 for $i = N + 1$ to $L - 1$ do $\mathbf{V}[i] = W^{-(L-i)^2/2}$
 $\mathbf{G} = \mathbf{Y} \otimes \mathbf{V}$ (using FFT convolution)
 for $i = 0$ to $N - 1$ do $\mathbf{G}[i] = \mathbf{G}[i] * W^{i^2/2}$
 return first N elements of \mathbf{G}

It can be verified that this will compute the necessary functions and perform the convolution of equation (8). In terms of computational complexity, the significant steps of this algorithm are the three L -point FFT operations used to evaluate this convolution. Each of these executes in $O(L \log L)$ time, and since $L = 2N$ in this application, this is equivalent to $O(N \log N)$, where N is the number of points in the transformed image.

3.2 Implementation of the DFT Using CZT

The following algorithm uses Algorithm 1 to calculate the DFT for SPRITE data, following the procedure outlined in Section 2.5.

Algorithm 2. (Computation of 1D Discrete Fourier Transform using CZT).

INPUT: An N_T by N_G matrix \mathbf{S} containing N_T time samples for each of the N_G gradient steps
 INPUT: An N_T -element vector **times** containing encoding times $t_p(j)$
 OUTPUT: The N_C -point nonuniform DFT of the dataset \mathbf{S}
 $N_C = N_G * N_T$
 let **out** and **sum** be empty N_C -element vectors
 for $j = 0$ to $N_T - 1$ do
 $T_j = \mathbf{times}[j] / \mathbf{times}[N_T - 1]$
 $\mathbf{out} = \text{CZT}(\mathbf{S}[j], N_C, T_j)$ (using Algorithm 1)
 $\alpha = \pi T_j / N_T$
 $\beta = -\pi T_j N_G / 2$
 For $k = 0$ to $N_C - 1$ do $\mathbf{out}[k] = \mathbf{out}[k] * e^{i(k\alpha + \beta)}$
 $\mathbf{sum} = \mathbf{sum} + \mathbf{out}$
 end for
 return **sum**

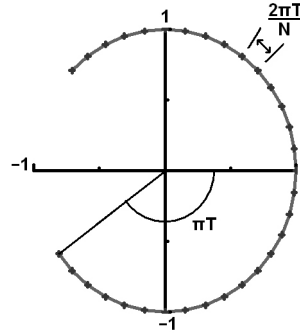


Fig. 4. The z -plane contour for FOV correction by a factor of T , $z(k) = e^{2\pi i k T_j / N_C - \pi i T_j}$.

This algorithm executes in $O(N_T N_C \log N_C + 2N_T N_C)$ time, since it calls Algorithm 1 and performs two $O(N_C)$ phase corrections, a total of N_T times. The asymptotic complexity is therefore $O(N_T N_C \log N_C)$. It should be noted that, if we use $N_C = N_G N_T$ as the number of points to calculate, this complexity becomes quadratic in N_T , which will significantly affect performance for large numbers of time samples.

While we will use $N_C = N_G N_T$ elsewhere in this paper to compare the accuracy of the algorithm with existing interpolation methods, in all practical applications we may safely set $N_C = N_G$, reducing the asymptotic complexity to $O(N_T N_G \log N_G)$ or $O(N_C \log N_C)$, as originally desired. This will compute a smaller image, and hence we refer to this modified version as the “nonexpanded” version of the algorithm, in contrast to the original “expanded” version which uses $N_C = N_G N_T$.

The nonexpanded version is constructed from the expanded algorithm by replacing N_C with N_G everywhere, including the equations of Section 2.4. This changes the linear phase correction to $\alpha' = \pi T_j$, but the data processing strategy is otherwise unaffected.

For example, if there are $N_G = 64$ gradient steps and $N_T = 4$ time samples collected at each gradient step, the expanded algorithm will compute a profile having $N_C = 256$ pixels. In contrast, the nonexpanded algorithm computes a profile of only $N_C = 64$ pixels. We will demonstrate in section 4 that this modification will provide superior speed for large numbers of time samples, but will not reduce the information content of the final image.

3.3 Generalization to Multiple Dimensions

The algorithms described in the previous two sections will process data in one dimension only. Since the majority of MRI data is two- or three-dimensional, the algorithms must be generalized to higher dimensions for use in practical applications. Fortunately, the separability of the Fourier transform allows us to use a succession of one-dimensional CZT operations to process data in multiple dimensions.

For example, in two dimensions, we have the following:

Algorithm 3. (Computation of 2D Discrete Fourier transform using CZT).

INPUT: An N_T by N_G by N_G array **S** of SPRITE MPA data
 INPUT: An N_T element vector **times** containing encoding times $t_p(j)$
 OUTPUT: The N_C by N_C nonuniform DFT of the dataset **S**
 let **start**, **stepA**, **stepB**, **sum** be empty N_C by N_C matrices
 for $j = 0$ to $N_T - 1$ do
 $T_j = \mathbf{times} / \mathbf{times}[N_T-1]$
 start = **S**[j]
 for $k = 0$ to $N_C - 1$ do
 stepA[k] = CZT(**start**[k], N_C , T_j) (using Algorithm 1)
 apply phase corrections to **stepA**[k] as in Algorithm 2
 end for
 stepA = transpose of **stepA**
 for $k = 0$ to $N_C - 1$ do
 stepB[k] = CZT(**stepA**[k], N_C , T_j) (using Algorithm 1)
 apply phase corrections to **stepB**[k] as in Algorithm 2
 end for
 stepB = transpose of **stepB**
 sum = **sum** + **stepB**
 end for
 return **sum**

In n dimensions, the total number of acquired samples will be $N_G^n N_T$. For the case of the nonexpanded algorithm, the number of time samples is arbitrary, within the limits discussed in section (2.3), and the number of calculated points is N_G^n , with $N_C = N_G$ points along each dimension. However, in the expanded case, the final size of the image remains $N_G^n N_T$, so there will be $N_C = N_G N_T^{1/n}$ points along each dimension. The number of time samples N_T must therefore be some integer raised to the power n , such that each dimension can be expanded equally and by an integral value.

The two-dimensional algorithm above calls Algorithm 1 a total of N_C times in each of the inner loops, and these in turn are computed N_T times—once for each of the collected time samples. The overall complexity is therefore $O(N_T N_C^2 \log N_C)$ for an N_C by N_C final image. In general, for an image of n dimensions each having size N_C , the asymptotic complexity is $O(N_T N_C^n \log N_C)$. As discussed earlier, this complexity is quadratic in N_T for the expanded case, but linear in N_T in the nonexpanded case.

4. RESULTS

The algorithms discussed in the previous section have been implemented and tested on a variety of multiple-point SPRITE MRI data. After verifying the calculated complexity of the algorithms, we will illustrate the ability of the CZT algorithm to enhance the quality of MRI images both in terms of signal-to-noise ratio and apparent resolution. Finally, the CZT algorithm will be compared

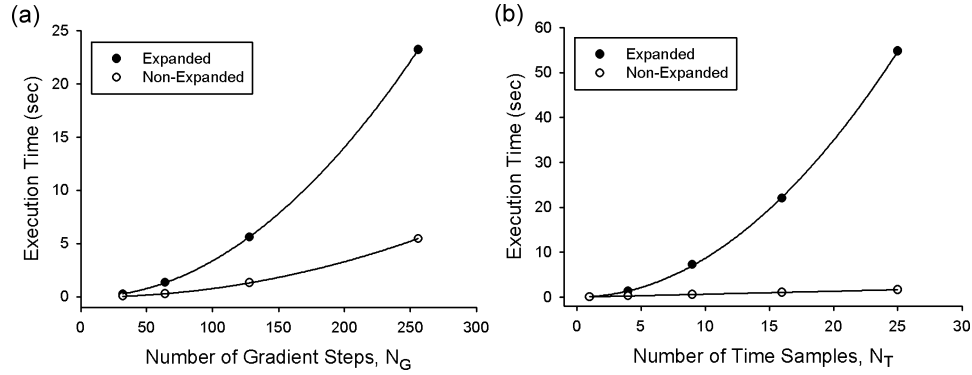


Fig. 5. (a) Dependence of CZT execution time on the number of gradient steps N_G in the SPRITE sequence. (b) Dependence of CZT execution time on the number of time samples N_T acquired at each step.

against the Dutt-Rohklin interpolation method to demonstrate its superior accuracy and decreased running time.

To provide a fair comparison, the expanded algorithm was used throughout this section except where otherwise stated.

4.1 Performance

We first demonstrate how the algorithm's execution time depends on the number of gradient steps N_G , which corresponds in turn to the size of the acquired k-space matrix, and on the number of time samples N_T acquired at each gradient step.

To this end, a number of MRI datasets were acquired, having various values of N_G and N_T , and these datasets were processed with both the expanded and the nonexpanded versions of the CZT algorithm. Figure 5(a) shows the execution time as a function of N_G with a fixed number of time samples ($N_T = 4$), while Figure 5(b) illustrates the algorithms' dependence on N_T with a fixed number of gradient steps ($N_G = 64$). This testing was performed on a 1.07 GHz Intel Celeron processor.

The dependence on the number of gradient steps is seen to be $O(N_G^2 \log N_G)$ for both versions of the algorithm, as expected. As can easily be seen, the running time for the nonexpanded algorithm with N_G steps matches the expanded algorithm with $N_G/2$ steps. The difference between the two algorithms is only made clear in the case of fixed N_G and varying N_T , in which the complexity of the expanded algorithm is shown to be quadratic in N_T , while that of the nonexpanded algorithm is linear.

4.2 Enhancement of MRI Data

Images processed with either of the CZT algorithms exhibit a noticeable increase in quality, mostly due to SNR improvement via signal averaging, which reduces the presence of random background noise. This can also lead to an apparent increase in resolution, such that smaller features which were

previously indistinguishable from the background now become visible. We shall demonstrate both of these effects by applying the algorithm to experimentally acquired MRI data.

First we illustrate the SNR improvement afforded by the algorithm. The sample chosen for this purpose is a fiber-reinforced polyester resin, a material which is of interest to the automobile industry for structural parts applications. This material has a naturally low MRI signal strength, and images of this material would generally require some signal-averaging to improve the SNR. However, this comes at a significant cost in terms of acquisition time, and SNR improvement with a CZT is desirable to provide a similar image more rapidly.

The sample was imaged using a 2.4T Nalorac horizontal bore superconducting magnet and a spiral SPRITE trajectory. The sample is cylindrical with a 19 mm radius and 8 mm in height. A 64×64 k-space matrix was acquired, and since resolution is not of great importance in this case, $T_{lim} = 0.6$ was selected, allowing 25 time samples to be collected under the constraint of equation (17). The field of view at $t_{max} = 325 \mu s$ is approximately 8 cm by 8 cm, and all processed images were scaled to this FOV so their SNR can be directly compared.

A number of images were acquired of this sample, each signal-averaged to a given extent during the acquisition, and processed with the CZT using a given number of time samples. Acquisition times for the three levels of averaging performed during the acquisition—1 scan, 4 scans, or 16 scans—were 6.5, 25, and 101 seconds respectively. The numbers of time points used were 1, 4, 9, 16, and 25; these values were chosen to meet the restriction that N_T must be a perfect square for the 2D Expanded algorithm.

The SNR for each of the images displayed in Figure 6 was obtained by calculating the average intensity of the central region, and dividing by the average intensity of a typical region in the background. See Table I and Figure 7.

As expected, the SNR of an image generally increases as the square root of the number of averages, but the source of the averaging has no meaningful impact. That is, the SNR improvement is independent of whether all averaging was performed during the acquisition (as in image **c**), with the CZT (as in image **j**) or in some combination of these two methods (image **e**). The only difference is the amount of time needed to acquire and process the images, which is lessened for multiple-point acquisition images processed by the CZT.

The polyester resin has no distinguishing features, so any extra resolution provided by the CZT would not be apparent. A different experiment was therefore performed to quantify the effect of CZT processing on the resolution. The sample was a circular resolution phantom made of crosslinked polybutadiene, containing holes and cuts of various sizes as shown in Figure 8. Following Equation (17), 9 samples were acquired at each gradient step.

Figure 9 illustrates the apparent resolution increase as more time samples are used in the CZT algorithm. Neither of the two smallest sets of holes are distinguishable in the original image, but all are visible in the image with $N_T = 4$, and are more sharply resolved with $N_T = 9$. (There is of course also a SNR benefit, which is the main source of the apparent resolution enhancement.)

The image with $N_T = 9$ was also processed with the nonexpanded version of the algorithm, and no loss in resolution was observed (image **d**), as evidenced

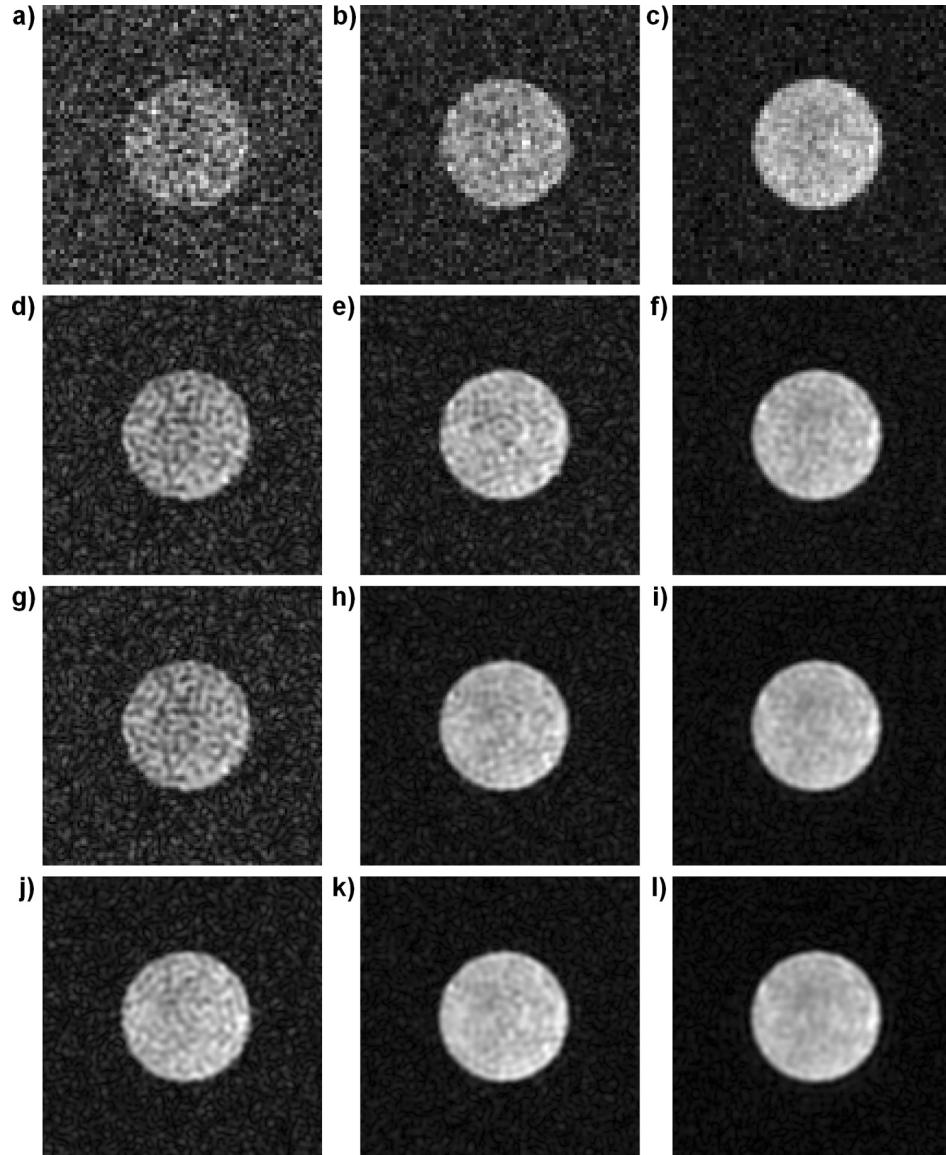


Fig. 6. SNR improvement of a 2D MRI image. Each column represents a different amount of signal averaging during the acquisition: 1, 4, and 16 averages respectively. Each row represents a different number of time samples used in CZT image reconstruction; 1, 4, 9 and 16 samples respectively. All images have a FOV of $8\text{cm} \times 8\text{cm}$.

by the fact that all features are still visible. This indicates that no information loss results from employing the nonexpanded CZT, even though the number of computed pixels is smaller. Though we will use the expanded algorithm in the next section for performing a comparisons with another algorithm, the nonexpanded algorithm presents itself as the best choice for most (if not all) practical applications in light of its lower computational complexity.

Table I. Image-Derived Signal-to-Noise Ratio Values for Various Numbers of Scans and Time Samples

| # Samples | SNR, 1 scan | SNR, 4 scans | SNR, 16 scans |
|-----------|-------------|--------------|---------------|
| 1 | 2.3 | 3.8 | 7.5 |
| 4 | 4.1 | 7.3 | 14.4 |
| 9 | 6.6 | 11.1 | 21.1 |
| 16 | 8.8 | 15.8 | 29.3 |
| 25 | 11.6 | 21.2 | 37.5 |

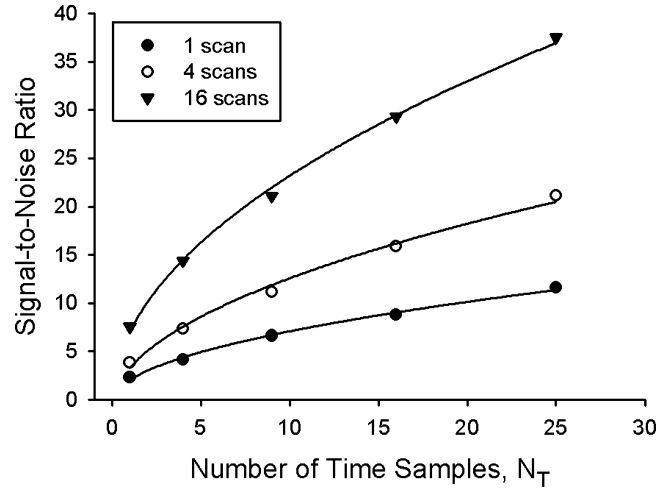


Fig. 7. SNR improvement due to signal averaging, in the form of extra scans during the acquisition, and by processing extra acquired time samples with the CZT.

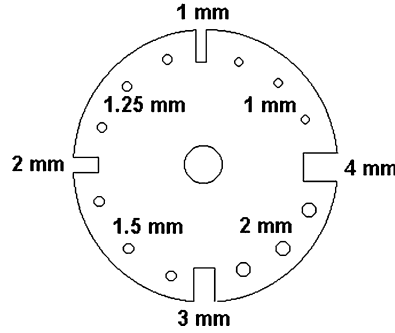


Fig. 8. Dimensions of the polybutadiene resolution phantom and its various features.

4.3 Comparison with Interpolation

The image enhancements demonstrated in the previous section are not unique to the CZT algorithm; if these datasets were processed with an interpolation method, the results would be similar. Indeed, in most cases they are visually indistinguishable. However, interpolation algorithms exhibit different complexity, and also provide varying levels of accuracy as compared to the explicit $O(N^2)$ form of the discrete Fourier transform. We will now compare the CZT to one

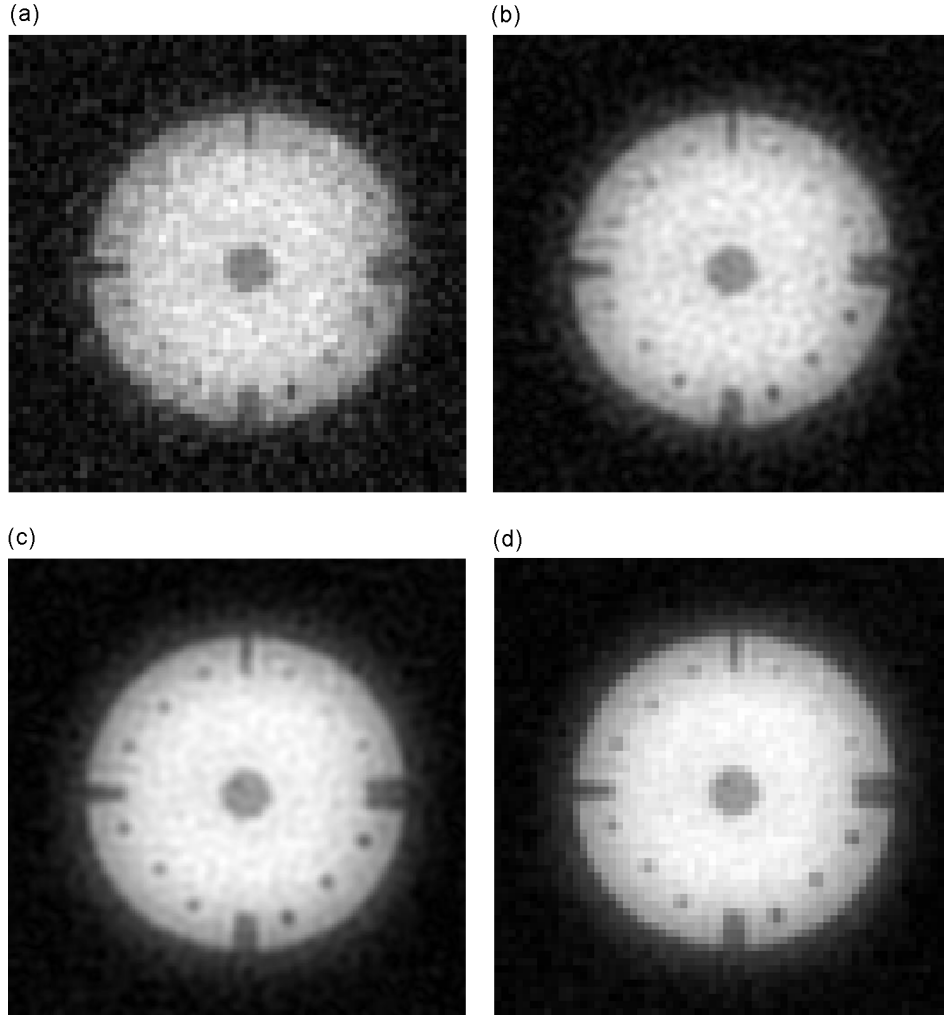


Fig. 9. Reconstructed images of the polybutadiene resolution phantom. FOV in all cases is approximately $6\text{cm} \times 6\text{cm}$. (a) Original image, $N_T = 1$. (b) Image reconstructed with expanded CZT and $N_T = 4$. (c) Image reconstructed with expanded CZT and $N_T = 9$. (d) Image reconstructed with nonexpanded CZT and $N_T = 9$. Though image (d) appears less smooth, the same features are visible, and therefore the resolution is the same as image (c) despite a smaller number of pixels reconstructed.

such algorithm, the interpolation method proposed by Dutt and Rokhlin [1993] and generalized to two-dimensional MRI data by Sarty et al. [2001].

The algorithmic complexity is stated as $O(mN \log N + mNq)$ for the one-dimensional case treated by Dutt and Rokhlin in their original paper [1993]. Here m is an oversampling parameter, usually set to 2, and q determines the accuracy of the calculation through the relationship $q = \lceil 4b\pi \rceil$, with b relating to the logarithm of the desired accuracy. The value $b = 0.6$ (and therefore $q = 8$) is suggested as reasonable for practical applications.

Table II. Mean Error (vs. Discrete Fourier transform) for CZT and the Dutt-Rokhlin (DR) Interpolation with Various values of the b Parameter, Which Controls the Accuracy of the Computation. (Sarty's extension of the Dutt-Rokhlin algorithm was used for two-dimensional data)

| Algorithm | Mean Rel. Error, 1D | Mean Rel. Error, 2D |
|---------------|-------------------------|------------------------|
| CZT | 4.00×10^{-16} | 5.85×10^{-14} |
| DR, $b = 0.6$ | 8.38×10^{-5} | 4.12×10^{-5} |
| DR, $b = 1.0$ | 8.57×10^{-7} | 1.08×10^{-6} |
| DR, $b = 2.0$ | 3.036×10^{-11} | 6.77×10^{-11} |
| DR, $b = 3.0$ | 4.4×10^{-15} | 6.54×10^{-14} |

Sarty et al. [2001] provided the logical extension of the algorithm to two dimensions, which operates in $O(mN^2 \log N + mN^2 q)$ time on a dataset containing N^2 points. This version, along with Dutt and Rokhlin's original 1D fomulation, have been implemented for comparison against the CZT in terms of speed and accuracy.

In addition to an image of the resolution phantom from the previous section (acquired with slightly different parameters, yielding a sharper image), a one-dimensional dataset from a prototype Electron Paramagnetic Resonance Imaging instrument [Goora 2003] was also used. Each was processed first with the Discrete Fourier Transform to provide a baseline for accuracy comparisons. The images were then reconstructed using both the Expanded CZT, and Dutt-Rokhlin or Dutt-Rokhlin-Sarty algorithm as appropriate. The Non-Expanded CZT was not used since the resulting image has fewer pixels than that generated by the DFT, and direct comparison is therefore not possible.

Speed and accuracy tests were conducted on a 1.07 GHz Intel Celeron processor. The accuracy of a given algorithm was quantified by subtracting the image reconstructed using that algorithm from the image reconstructed by the DFT, and then dividing by the magnitude of the DFT image to obtain a relative error for each pixel. The mean values of this error are listed in Table II.

The one-dimensional case of Figure 10 clearly illustrates a difference in the accuracy of the two methods. As claimed, the CZT allows computation of the DFT to considerable accuracy, on the order of the machine epsilon for double-precision floating-point arithmetic, $\epsilon_{mach} \sim 10^{-16}$. In contrast, using the suggested value of $b = 0.6$ for the Dutt-Rokhlin algorithm yields an accuracy of only 10^{-5} . This accuracy can be improved by increasing b , but the execution time will increase steeply as a consequence.

As observed in section 3.3, the two-dimensional CZT is a succession of one-dimensional CZT operations, and some errors will accumulate throughout the transform. However, the observed difference between the CZT and DFT in the two-dimensional case is still small, usually on the order of 10^{-14} or 10^{-13} , as shown in Figure 11. The Sarty algorithm continues to provide accuracy only on the order of 10^{-5} to 10^{-4} for the default value of b . As with the previous case, increasing b will improve the accuracy at a cost in terms of execution time.

Figures 10(d) and 11(d) summarize the results of the testing; these plots of accuracy as a function of execution time clearly illustrate that the CZT is preferable to this interpolation method in all cases. Low values of the interpolation

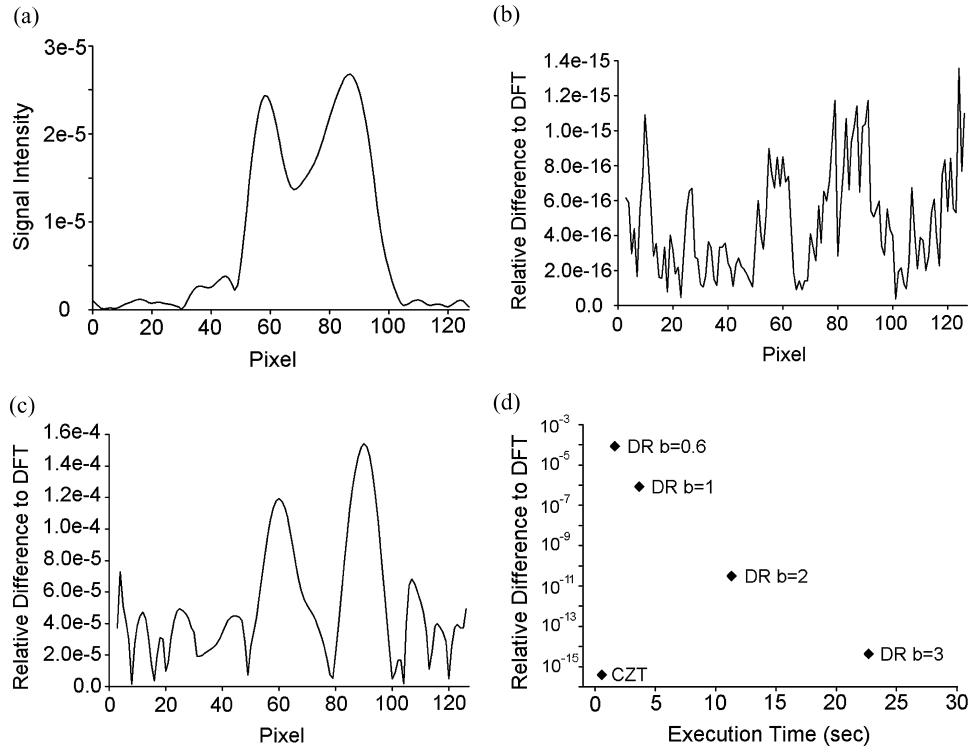


Fig. 10. Comparison of the Dutt-Rokhlin and CZT reconstructions for a 1D EPRI image, $N_G = 32$, $N_T = 4$. (a) Image as reconstructed by DFT. (b) Differences between the DFT and CZT. (c) Differences between the DFT and Dutt-Rokhlin algorithm with $b = 0.6$. (d) Accuracy and running time for various reconstructions.

parameter b yield comparable execution speeds but greatly reduced accuracy, while high b values that permit accuracy on the order of the machine epsilon increase the execution time significantly—by a factor of almost 50.

5. CONCLUSIONS

In this article we have presented an alternative method for computing the discrete Fourier transform of MRI data acquired with the SPRITE family of imaging techniques. This method employs the chirp z-transform algorithm, which has already been demonstrated as a useful tool for correcting the different fields of view for data acquired with multiple-point acquisition. We have shown that this same algorithm can be used, in combination with a set of phase corrections, to implement the DFT to very high accuracy in $O(N \log N)$ time. The CZT is readily generalized to multiple dimensions for processing 2D and 3D MRI data.

MRI images processed with the CZT exhibit significant improvement due to increased SNR. The application of this algorithm to the imaging of materials having naturally low MRI signal strength is clear. It may also find applications in the imaging of dynamic systems where measurement speed is important; signal averaging can be shifted to the post-processing stage to decrease

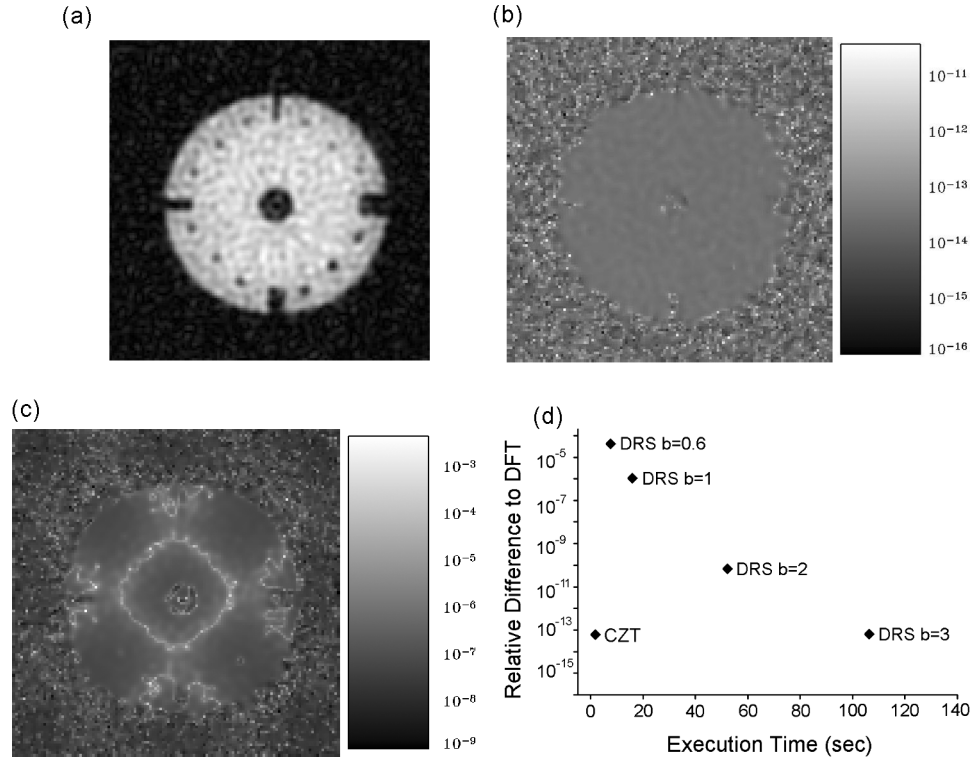


Fig. 11. Comparison of the Dutt-Rokhlin-Sarty and CZT reconstructions for a 2D image, $N_G = 64$, $N_T = 4$. (a) MRI image as reconstructed by DFT. (b) Differences between the DFT and CZT. (c) Differences between the DFT and Dutt-Rokhlin-Sarty algorithm with $b = 0.6$. (d) Accuracy and running time for various reconstructions.

acquisition time without sacrificing image quality. We anticipate that these ideas will be of value for niche applications in clinical MRI using pure phase encode techniques.

Interpolation methods can achieve qualitatively similar results to the chirp z-transform, but the CZT provides significant advantages over these methods. It computes the DFT more accurately and in less time than the Dutt-Rokhlin interpolation method, or its two-dimensional equivalent. Our tests have demonstrated the increased performance of the expanded version of the algorithm; it follows that the nonexpanded algorithm will provide an even greater execution time savings for datasets with large numbers of time samples, and with no loss in overall image quality.

It should be noted that interpolation methods such as Dutt-Rokhlin are more generally applicable than the CZT. The mathematical formulation presented in this paper makes some assumptions about the structure of the data—specifically, that the gradient values G_k at any given time be uniformly spaced. Interpolation methods are not restricted in this way and are therefore applicable to non-Cartesian acquisition patterns, such as spirals, for which the CZT approach would be unsuitable. However, no restriction exists on the time points

t_p ; while our particular system acquires uniformly spaced time points, any distribution of t_p is possible. The only limitation for SPRITE MRI applications is that the number of time points should not exceed Halse's limit (Equation 17).

For most applications in MRI, the enhanced accuracy of the chirp z-transform is not as critical a consideration as the decreased running time. However, the reformulation of the DFT in terms of a set of CZT operations may have other applications, most notably the numerical solution of differential equations on non-uniform meshes containing regularities similar to those of the SPRITE sampling pattern. In such an application, the high accuracy of the algorithm would become important.

REFERENCES

- BALCOM, B., MACGREGOR, R., BEYEA, S., GREEN, D., ARMSTRONG, R., AND BREMNER, T. 1996. Single point ramped imaging with T1 enhancement (SPRITE). *J. Magn. Reson. A* 123, 131.
- BLUESTEIN, L. 1968. A linear filtering approach to the computation of the discrete Fourier transform. *Northeast Electronics Research and Engineering Meeting Record* 10, 218.
- COOLEY, J. AND TUKEY, J. 1965. An algorithm for the machine calculation of complex Fourier series. *Math. Comp.* 19, 297.
- DUTT, A. AND ROKHLIN, V. 1993. Fast Fourier transforms for nonequispaced data. *SIAM J. Sci. Comput.* 14, 1368.
- GOORA, F. G. 2003. Electron paramagnetic resonance imaging using a pure phase encode technique. M.S. thesis, University of New Brunswick.
- HALSE, M., GOODYEAR, D., MACMILLAN, B., SZOMOLANYI, P., MATHESON, D., AND BALCOM, B. 2003. Centric scan SPRITE magnetic resonance imaging. *J. Magn. Reson.* 166, 219.
- HALSE, M., RIOUX, J., ROMANZETTI, S., KAFFANKE, J., MACMILLAN, B., MASTIKHIN, I., SHAH, N., AUBANEL, E., AND BALCOM, B. J. 2004. Centric scan SPRITE magnetic resonance imaging: Optimization of SNR, resolution and relaxation time mapping. *J. Magn. Reson.* 169, 102.
- JACKSON, J., MEYER, C., NISHIMURA, D., AND MACOVSKI, A. 1991. Selection of a convolution function for fourier inversion using gridding. *IEEE Trans. Med. Imaging* 10, 473.
- KAFFANKE, J., DIERKES, T., ROMANZETTI, S., HALSE, M., RIOUX, J., LEACH, M. O., BALCOM, B., AND SHAH, N. J. 2005. Application of the chirp z-transform to MRI data. *J. Magn. Reson.* (submitted).
- LIU, Q. AND NGUYEN, N. 1998. An accurate algorithm for nonuniform fast Fourier transforms (NUFFT's). *IEEE Microwave and Guided Wave Letters* 8, 18.
- MEYER, C., HU, B., NISHIMURA, D., AND MACOVSKI, A. 1992. Fast spiral coronary artery imaging. *Magn. Reson. Med.* 28, 202.
- NGUYEN, N. AND LIU, Q. 1999. The regular Fourier matrices and nonuniform fast Fourier transforms. *SIAM J. Sci. Comput.* 21, 283.
- PASCHAL, C. B. AND MORRIS, H. D. 2004. K-space in the clinic. *J. Magn. Reson. Imag.* 19, 145.
- PRADO, P. J., BALCOM, B. J., MASTIKHIN, I. V., CORSS, A. R., ARMSTRONG, R. L., AND LOGAN, A. 1999. Magnetic resonance imaging of gases: A single point ramped imaging with T₁ enhancement (SPRITE) study. *J. Magn. Reson.* 137, 324.
- RABINER, L., SCHAFER, R., AND RADER, C. 1969. The chirp z-transform algorithm. *IEEE Trans. Audio Electroacoustics* 17, 86.
- RIOUX, J. 2003. Nonuniform fast Fourier transformation of SPRITE MRI data.
- SARTY, G., BENNETT, R., AND COX, R. 2001. Direct reconstruction of non-Cartesian k-space data using a nonuniform fast Fourier transform. *Magn. Reson. Med.* 45, 908.
- SHA, L., GUO, H., AND SONG, A. 2003. An improved gridding method for spiral MRI using nonuniform fast Fourier transform. *J. Mag. Reson.* 162, 250.

Received July 2005; revised June 2006; accepted August 2006